ASSESSMENT OF ERROR ESTIMATION METHODS WITH AN EMPHASIS ON LOCAL ERROR IN APPLIED FLOWS

R. Mörsch*, E. Tangermann*, M. Klein*

* Institute of Applied Mathematics and Scientific Computing Bundeswehr University Munich, Werner-Heisenberg-Weg 39, 85577 Neubiberg, Germany

Abstract

The capabilities of a-posteriori discretisation error estimation methods is investigated with an emphasis on local flow variables in aerodynamic flows. Sets of meshes are generated for three different test cases that represent typical aerodynamic flow features. Simulations are carried out using the TAU-Code solver developed by the German Aerospace Center (DLR).

Performance of the estimation methods to locate the error correctly is first judged by visual inspection. In addition, a quantitative error measurement is introduced to validate the accuracy of the magnitude estimation. Ultimately, the study aims to lay a foundation for error estimation in complex geometries and provides a basis for grid requirements and local grid refinement.

Keywords

mesh refinement; discretisation error; uncertainty quantification; local error estimation

NOMENCLATURE			Abbreviations	
Symbols			EE	Error estimation
α	Angle of attack	\deg	GCI	Grid convergence index
C_D	Drag coefficient	-	RE	Richardson extrapolation
C_L	Lift coefficient	-		•
C_{MY}	Pitching moment coefficient	-	1. INTRO	DDUCTION
C_{MZ}	Yawing moment coefficient	-	Recent advances in computational capabilities have transformed computational fluid dynamics (CFD) into an indispensable tool across a variety of different industries. Especially in aerospace, high operational costs of wind tunnels and flight tests drive the endeavour towards virtual certification through simulation. However, CFD results are still subject to multiple er-	
C_P	Pressure coefficient	-		
E	Absolute error	-		
ϵ	Relative error	-		
h	Grid size indicator	-		
M	Mach number	-		In an effort to quantify errors in computences, the subject dealing with verification
N	Number of grid points	-	and validation has emerged [1, 2]. In addition, error estimation has been deemed one of the key challenges in NASA's CFD Vision 2023 road map [3]. The current study investigates the ability of different estimation methods to accurately predict the location and magnitude of the discretisation error in local flow	
p	Pressure	Pa		
ϕ	Arbitrary solution variable	-		
r	Grid refinement ratio	-		
u	Stream-wise velocity	m/s	variables.	For this purpose a set of grids is created for
Indices			flows: sepa	ent test cases featuring typical aerodynamic arated, transsonic and vortical flows. The ce comparison of error estimations is carried
e	Estimate		out for the original grid convergence index (GCI) [4], a novel local variation, and the approximate error scaling method [5].	
∞	Free-stream condition			
t	True		-	

2. NUMERICAL ERROR ESTIMATION

Today it is well established that the numerical error can be further subdivided into round-off, iterative and discretisation errors [1]. Round-off errors are universal to all computational tasks and are caused by the finite precision of computers, they are unavoidable. Fortunately, their magnitude is small compared to the other error sources and their influence on the solution can be neglected. Iterative errors describe the difference between a theoretically completely converged solution on a mesh and the presented solution at the current iteration. For engineering applications, a converged solution can typically be obtained by careful monitoring of residuals or specific engineering metrics, e.g. force or momentum coefficients. The largest proportion of numerical error is caused by numerically solving the governing equations in the discretised computational domain. Most studies across literature focus on the last error type when they talk about the estimation of numerical error [6–8].

The common goal for all discretisation error estimation (EE) methods is to predict the difference between a solution variable ϕ computed on an existing grid and the exact solution to the formulated problem. The exact solution can be replaced with a numerical solution on a grid with an infinitesimally small grid size parameter h. The true error $E_t(\phi, h)$ can be computed by assuming the following relationship:

(1)
$$E_t(\phi, h) \propto a \cdot E_a(\phi, h),$$

where $E_a(\phi,h)$ is the approximated error and a a proportionality constant. As mentioned above, the true error is defined as $E_t(\phi,h)=\phi(h=0)-\phi(h)$. The estimated error can be computed from $E_e(\phi,h)=\phi(h)-\phi(r\cdot h)$ but requires at least two solutions on grids with different cell sizes. The variation in cell size is expressed through the refinement ratio $r=h_2/h_1$ which is defined as the ratio of the grid size parameter. In the present study, the subscript 1 refers to the finest grid and subsequent subscripts describe coarser grids. The solution variable ϕ can refer to a local flow quantity defined per cell as well as integral values.

First efforts to estimate a solution on a grid with a theoretical grid size of zero were made by Richardson and Gaunt [9]. Richardson Extrapolation (RE) uses the following equation to solve for the solution on a grid with infinitesimal small spacing $\phi(h=0)$

(2)
$$\phi(h) = \phi(h = 0) + C \cdot h^p + t.h.o.$$

The three unknowns in Eq.2 require solutions from three differently fine grids to determine the solution of the equation system. Rearranging the equation leads to the formulation of the GCI [4] that is widely used to report the discretisation error in CFD studies

(3)
$$GCI_1 = \frac{F_s|\epsilon|}{1 - r^p}$$
 $GCI_2 = GCI_1r^p$

with the safety factor F_s and the relative error ϵ . The GCI_1 describes the error on the fine grid and the subscript 2 refers to the error on the coarse grid. To reduce the number of grids necessary to obtain an error estimate, one can assume that the order of convergence p matches the formal order of the numerical scheme employed to obtain the solution. Then only two grids are needed to compute the GCI. Additionally, it should be noted that the determination of p can be a challenge by itself [10]. Therefore, the results presented in the current study were computed assuming the formal order of convergence. For the computation of the GCI with two grids, the factor of safety F_s is set to three to obtain a conservative error estimate.

Across literature, the GCI is often applied to integral values, e.g. force coefficients. These global variables are of great interest for engineering application. Yet, additional information of the local error can help to setup suitable meshes for efficient simulations.

The cell-wise application of the GCI leads to issues with the relative error ϵ . Near a wall or in region of flow re-circulation, the relative error may lead to spurious results due to division by small values. However, these areas are often of particular interest for aerodynamic flows. To avoid this issue, the present study uses the absolute error to compute the GCI. Strict requirements for the grid generation process hinder the GCI to be applied to complex geometries if all theoretical prerequisites should be met. To circumvent some of these prerequisites, a local GCI variant is introduced. The idea behind this method is to obtain a local grid refinement ratio by defining a "radius of interest" around each cell. A refinement ratio can be calculated when treating the area(2D)/volume(3D) inside the radius as an independent grid. By setting the correct size for the radius, each small section satisfies the condition of uniform grid refinement. One drawback of this method is that the determination of the cells that lay within the interest area can become computationally expensive for very larger unstructured grids.

An alternative methodology to find the proportionality constant a between the true and estimated error, the approximate error scaling (AES) method was proposed in [5]. In contrast to the well established RE, the procedure completely avoids the use of a grid sizing parameter or refinement ratio and does not require any knowledge about the order of convergence. The absence of any measure for the cell size makes the AES method a promising alternative for error estimation on unstructured-hybrid grids.

On the downside, the method requires a set of at least three grids to compute a defined as

(4)
$$a = \frac{||a_i^1||_1 + ||a_i^2||_1}{2N},$$

where a_i^1 and a_i^2 are local variables computed at every grid point i. The global constant a is defined as the average of the local variables across the total number of cells N.

(5)
$$a_i^1 = \frac{\phi_2^i - \phi_1^i}{\phi_3^i - 2\phi_2^i + \phi_1^i}$$

and

(6)
$$a_i^2 = \frac{\phi_3^i - \phi_2^i}{\phi_3^i - 2\phi_2^i + \phi_1^i}.$$

In order to judge the performance of the different error estimation methods, qualitative inspection of the results is not sufficient. It can provide useful insight into the error location, but lacks the capability to draw accurate conclusions about the magnitude of the error. To do so, the current study combines the location and magnitude of the estimated error into a single metric using the ℓ_1 -norm. It is defined as

(7)
$$||x||_1 = \sum_{i=0}^{N} |x_i|,$$

where x_i represents an error variable at each grid point and N the total number of cells.

2.1. Challenges

Even though today discretisation error estimation is widely used, its application is still associated with a number of challenges.

2.1.1. Reference solution

Key to evaluate the performance of error estimation methods is the existence of a suitable reference solution. Typically, proposed error estimation schemes are tested against generic scalar transport equations or simple flows which have an analytical solution [5], [11]. Engineering problems often feature complex flows that can only be solved numerically. To circumvent this problem, a very fine mesh was generated in addition to the set of meshes for the error estimation. This really fine mesh acts as a numerical reference solution to evaluate the performance of the estimation scheme. It is acknowledged that the reference solution is not free of discretisation errors itself. However, using a numerical reference with the same modeling approach provides the benefit that modelling errors do not need to be considered explicitly unlike when using a reference form an experiment or a high-fidelity computation.

2.1.2. Grid related concerns

As previously mentioned, test cases often feature very basic geometries and flows to reduce complexity. To add to the simplicity, they are often two-dimensional. This allows to discretise the geometry using structured grids with quadrilateral cells that enable easy refinement to create a series of grids needed to conduct an error estimation study. The transition to complex ge-

ometries that feature unstructured hybrid grids brings along some challenges:

- Generating a set of grids that satisfies requirements for EE-schemes
- Treatment of the near-wall and far-field regions
- Determining a characteristic cell size

2.1.3. Data Interpolation

In order to analyse the results of the different meshes, solution variables have to be interpolated onto a common grid. For the two-dimensional test cases as well as the surface values, the data from all solutions is linearly interpolated onto the coarse grid. For the analysis of the flow field of the three-dimensional grid, planes are extracted using structured rectangular grids in areas of interest. It is assumed that the error introduced by interpolation is sufficiently small and can therefore be neglected.

3. GRID GENERATION

Creating a good quality group of meshes is essential to carry out error estimations. The following section briefly discusses how the meshes for all test cases were created and explains the choices made during grid generation.

For aerodynamic flows it is especially important to accurately capture the flow in the near wall region. For wall-resolved simulations, a common practice is to choose the height of the first cell to match $y^+=1$. This principle was also applied in the present study. Additionally, inflation layers are used to discretise the near-wall regions in a computationally efficient way. For each test case the coarsest grid serves as a starting point for the grid generation and satisfies the $y^+=1$ condition. The procedure to create subsequent meshes is as follows:

- The height of the first prism cell is kept constant at $y^+ = 1$ for all meshes. Additional refinement would lead to increased computational cost without any accuracy gain.
- A global cell size is specified and the number of prism layers is adjusted to obtain a smooth transition between prismatic and hexahedral cells.
- Cell size is scaled by a factor of $1/2^{\frac{n}{2}}$, where n is the number of grid dimensions.

While this procedure does not result in a set of completely scaled meshes, it is typical for engineering problems.

4. FLOW SOLVER AND TEST CASE SETUP

Simulations are performed using the DLR TAU-Code release.2021.1.0 flow solver developed by the German Aerospace Center [12]. TAU is a second order finite volume flow solver that is optimised for the use on unstructured hybrid grids. For all test cases in the present study, the Spalart-Allmaras turbulence model [13] with negative correction is employed to close the

RANS equations. The model is widely used in aerodynamic applications and solves the following transport equation

(8)
$$\frac{\partial \tilde{\nu}}{\partial t} + \vec{u} \cdot \vec{\nabla} \tilde{\nu} = c_{b1} (1 - f_{t2}) \hat{S} \tilde{\nu} - \left[c_{w1} f_w - \frac{c_{b1}}{\kappa^2} f_{t2} \right] (\frac{\tilde{\nu}}{d})^2 + \frac{1}{\sigma} \left[\vec{\nabla} (\nu + \tilde{\nu}) \vec{\nabla} \tilde{\nu} + c_{b2} \vec{\nabla} \tilde{\nu} \right].$$

For negative values of $\tilde{\nu}$, the formulation proposed by [14] is solved instead.

Three different test cases have been carefully selected to reproduce flow phenomena present in typical external flows. Namely, these are separated, transonic and vortical flows. The first two test cases are two-dimensional simple cases used to evaluate the applicability and performance of the aforementioned methods. The last test case serves as a trial for error estimation in complex three-dimensional flows.

4.1. Case 1: Separated flow over a hump

The NASA wall mounted hump geometry is part of a series of thoroughly investigated test cases provided by NASA that are used to validate turbulence models. A detailed overview of the setup is provided in [15]. The computations are run at a free-stream Mach number $M_{ref}=0.1$ with a Reynolds number of 936000. Simulations are performed on four different unstructured meshes ranging from N=10142 to N=77270 cells. A structured grid with 1632 cells in stream-wise and 432 in the wall-normal direction taking from the NASA turbulence modelling data base acts as a basis for the reference solution. The grid is available at [16].

4.2. Case 2: NACA0012 airfoil

The NACA0012 airfoil is part of the NACA four-digit series and resembles a symmetric airfoil with a maximum thickness equal to 12% of it chord length. The setup consists of a c-shaped computational domain with a far-field boundary conditions applied to the edges. The free-stream mach number M_{∞} equals 0.75. Simulations are performed at a Reynolds-number of $Re = 10^7$. A previous study by [17] revealed the existence of shock buffet for angles of attack exceeding 3.8°. Since discontinuities itself are already challenging, steady simulations are performed at $\alpha = 3.5^{\circ}$ to avoid buffet and obtain a stationary shock. Five different grids are generated by modifying the aspect ratio of the first prism cell while keeping the height constant at $y^+=1$. The result is a set of grids that range from 63k to 484k cells. The reference solution is obtained on a grid that has a highly refined region above the airfoil to accurately capture the shock and consists of approximately 3M cells.

4.3. Case 3: Flow around VFE-2

The final test case introduces three-dimensional vortical flow to the challenge of error estimation. The

vortex flow experiment (VFE-2) geometry features a 65° swept delta wing. The geometry has been extensively investigated in previous studies [18]. To keep complexity at a minimum, simulations are carried out at subsonic conditions with a free-stream Mach number $M_{\infty} = 0.4$, Reynolds number $Re = 3 \cdot 10^6$ and an angle of attack $\alpha = 13.3^{\circ}$ to ensure vortex formation but avoid vortex breakdown. To allow for a simple grid generation, the geometry features a leading edge with a medium sized radius equal to that found in [18]. In addition, the sharp trailing edge is also modelled with a slight radius. Due to the symmetric nature of the geometry, the computational domain only features a half wing. This way the computational cost can be significantly reduced. A set of three meshes with 4.4M, 9.6M and 21.3M nodes is created in addition to a reference mesh that consists of 110M nodes. All meshes feature a refined region around the wing and a relatively coarse mesh in the far-field.

5. RESULTS

The next section will present the findings of the study and will provide insight into the performance of the different estimation schemes when applied to a set of flow conditions.

5.1. Wall-mounted hump

The flow field over the wall mounted hump acts as a first benchmark case to test the applicability and performance of the previously discussed methods. Figure 1 compares the error norm of the stream-wise velocity u and pressure p across the whole computational domain according to equation 7. The four bars represent the "true" reference error and the three error estimates based on the GCI, its local variant and the AES. The norm is a measure for the accumulated error across the whole computational domain. This means that the magnitude of the estimation should match the reference error. It becomes clear that the local GCI variant performs worst across the whole range of grids by a significant margin, especially for the pressure error.

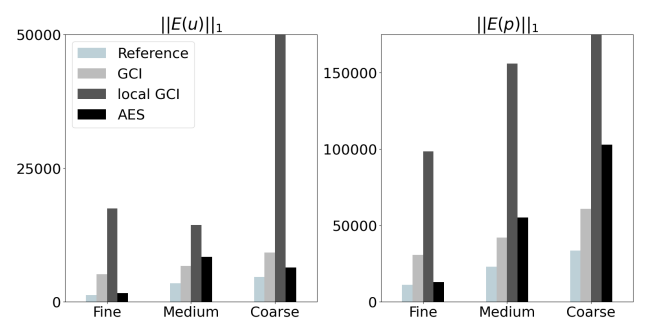


FIG 1. Error norm for the stream-wise velocity (left) on the left and pressure (right).

However, Figure 1 does not tell the full story. In theory, the error estimation is able to predict the accurate error magnitude across the domain, but could do

so by locating the error at the wrong position in the grid. This concern can be addressed by forming the difference between the reference and estimated error before plotting the norm. The results are presented in Figure 2. An accurate prediction of the error is indicated by a low overall error norm. An ideal overlap between the reference and estimated error would results in $||\Delta E(\phi)||_1 = 0$. Again, the local variant of the grid convergence index is vastly underperforming compared to the other two methods. Between the other two, the AES scheme has a slight edge over the GCI for the fine meshes. For the pressure error its performance falls of quickly on the coarser meshes.

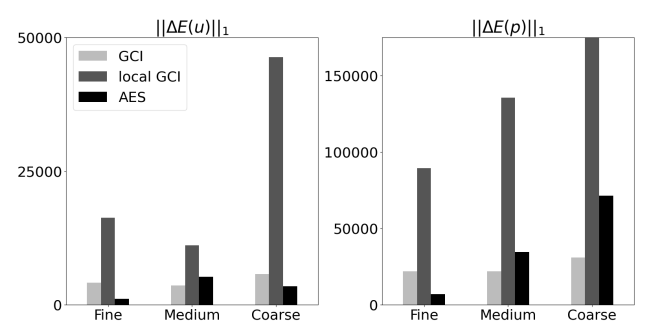


FIG 2. Error norm for difference in error between reference and estimation. Stream-wise velocity on the left and pressure on the right.

Concluding, the performance of the local GCI variant is deemed to poor. In addition, this method becomes increasingly computationally expensive for larger unstructured grids. Therefore, it is decided to not investigate the method further for the other test cases.

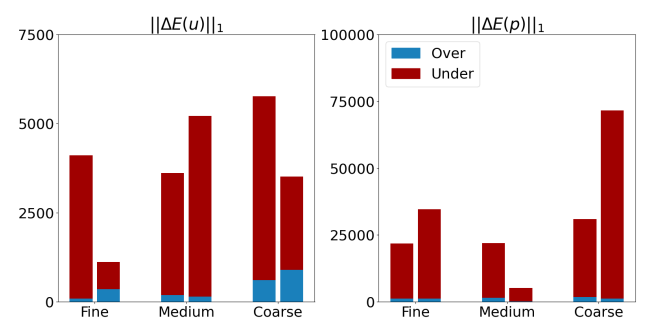


FIG 3. Error norm for difference in error between reference and estimation divided into over- and under prediction. The left bar shows the GCI and the right bar the AES method. Stream-wise velocity on the left and pressure on the right.

A last important distinction is presented for the difference in magnitude between "true" and estimated error. For practical applications, overpredicting the error is better than underprediction. Figure 3 displays the share of error that is over- and under predicted by the GCI and AES error estimation method. Both predict the magnitude of the error smaller than it really is across all grids and investigated flow variables.

5.2. NACA 0012

The two-dimensional NACA0012 airfoil confronts the error estimation methods with a particular challenging flow phenomenon: a discontinuity introduced by a shock above the airfoil. It is expected that the position of the shock moves based on the grid resolution. This has a significant influence on the pitching moment coefficient. Figure 4 presents the evolution of the lift and pitching moment coefficient on the left and right side respectively. Both variables show asymptotic behaviour and approach their limit value with increasing grid resolution.

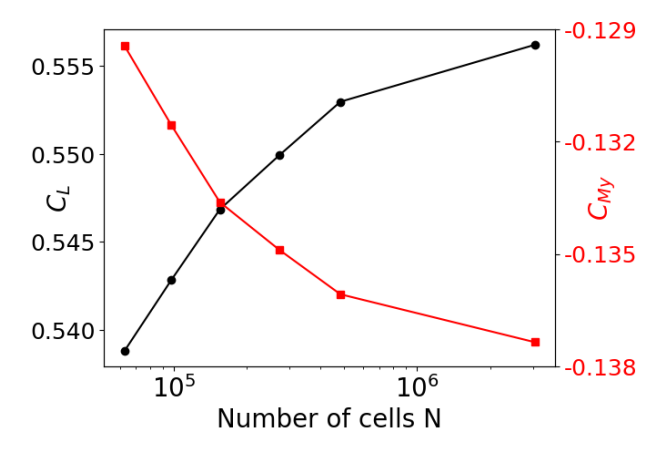


FIG 4. Lift and pitching moment coefficient of NACA0012 airfoil plotted against grid resolution.

Before the performance of the error estimation schemes is discussed, the flow field and reference error are presented in Figure 5. The top contour shows the Mach number distribution above the wing. A close up of the shock origin on the airfoil surface at $x/c \approx 0.41$ in Figure 5 [c] shows the lambda structure of the shock system, revealed in more detail by computing the error. As expected, the error is almost exclusively located at the alleged shock location and pictures a perfect representation of the discontinuity. Upand downstream of the shock, the Mach number is relatively uniform and accurately predicted even by the coarse grids.

CC BY-SA 4.0

5

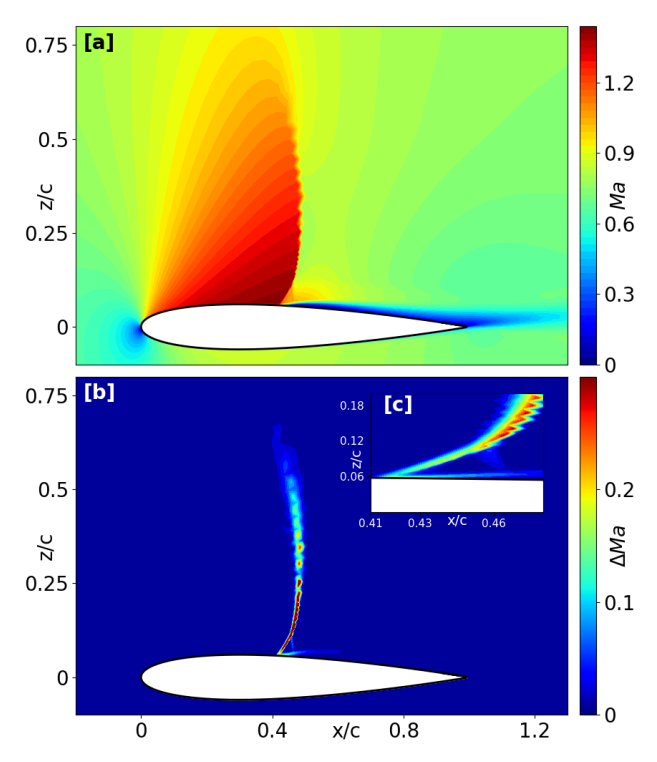


FIG 5. Contour plots of Mach number [a], reference error on medium grid [b] and close-up of lambda structure visualized through the error [c].

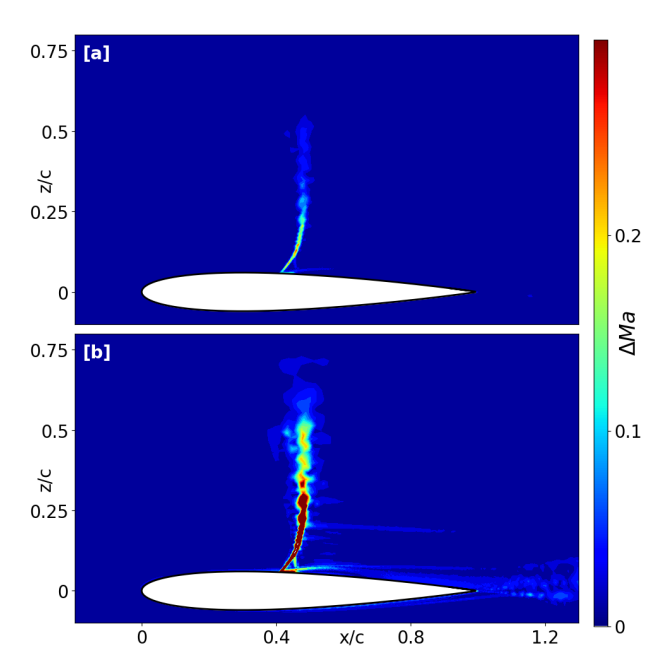


FIG 6. Contour of estimated error using [a] the GCI and [b] the AES method.

Figure 6 shows the estimated error. The top contour displays the grid convergence index, the AES method is presented in the bottom. By visual inspection both methods predict the error at the correct location. However, both estimations fail to capture the curvature of the shock above z/c=0.25. The GCI underestimates the magnitude slightly, especially right above the wing. Contrary, the AES method provides a very conservative estimate and significantly overpredicts the error magnitude.

Ultimately, the capability to deal with discontinuities can only be judged by looking at a quantitative evaluation of the results. In alignment with the results from the flow field analysis, the AES method seems to vastly overestimate the error for Mach number across the whole range of grids as displayed in figure 7. In particular for the fine grid the method estimate a very high error magnitude in comparison to the reference. The right-hand side of Figure 7 displays the estimation discrepancy for ν_t . For the turbulent viscosity, the error estimate from the two methods shows equal performance across the whole range of grids..

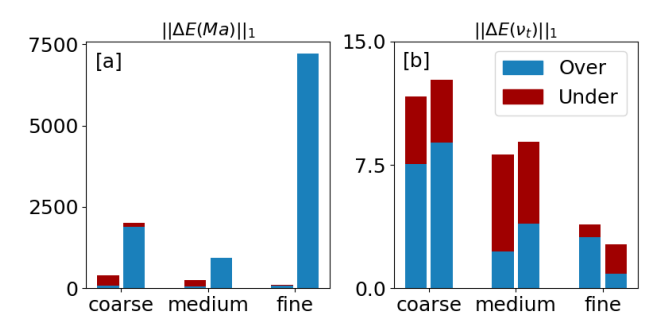


FIG 7. Difference in reference and estimated error norm for three different grids. Part [a] displays the norm for the error in Mach number and [b] for turbulent viscosity. The left bar represents the GCI and the right bar the AES estimation.

5.3. VFE-2

As previously discussed, sufficient resolution is necessary in order to carry out a meaningful grid study. Therefore asymptotic behaviour is verified for selected aerodynamic coefficients. Figure 8 shows the evolution of the drag and yaw-moment coefficient for the VFE-2 geometry in dependence of the number of grid points per mesh. Both coefficients show clear asymptotic behaviour and approach a grid-independent limit. Consequently it is assumed that all grids have a high enough resolution for a valid study.

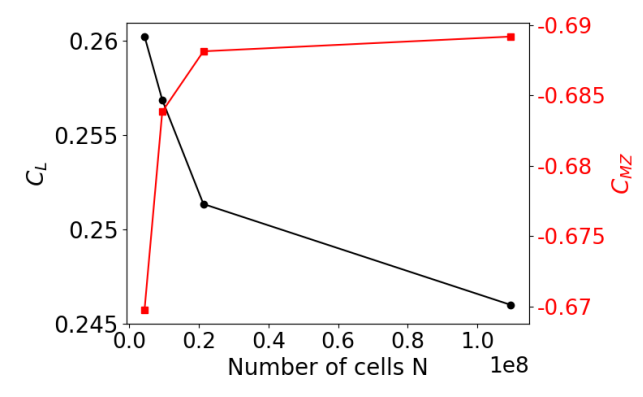


FIG 8. Grid dependency of the drag and yaw-momentum coefficient

For aeronautical applications, especially the development of delta-wing aircraft, the surface pressure distribution plays a crucial role since all aerodynamic forces

and moments are computed based on C_P . Figure 9 highlights the grid-related differences in the C_P distribution. Especially on the coarse grid, the strength of the suction footprint of the outward leading edge vortex is underpredicted. The region of strong negative pressure ends at a stream-wise location of approx. x/c = 0.65, whereas the fine and reference mesh extend the region up to x/c = 0.8. This discrepancy is also highlighted by the error estimation. Additionally it can be observed, that the footprint of the primary vortex is not captured with decreasing cell density. In Figure 9, the dash-dotted line represents the vortex core of the primary vortex. It can be seen that only the fine grids are able to predict the low-pressure area between x/c = 0.7 and 0.8.

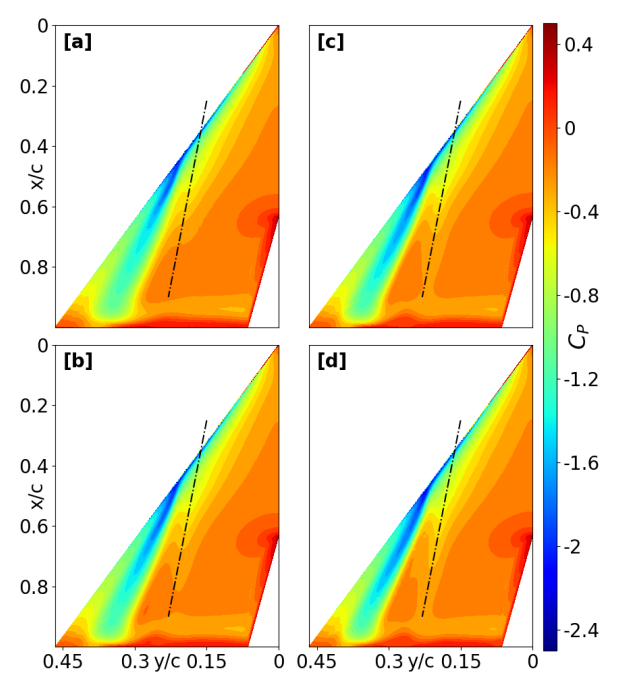


FIG 9. Pressure coefficient C_P distribution on the upper side of the wing computed on the coarse [a], medium [b], fine [c] and reference [d] mesh.

The mesh induced error is presented in Figure 10 [a]. Sub figure [b] displays the estimated error obtained by calculating the GCI and lastly [c] shows the estimation through the AES method. Both schemes are able to capture the overall shape and location of the surface pressure error well. Comparing the magnitude of the estimated error, severe differences become visible. The GCI is able to predict the error magnitude in C_P with good accuracy. On the contrary, the AES scheme results in a over conservative estimate and significantly overestimates the error magnitude. This is confirmed by looking at [d]. The two bars show the norm of the difference in error between the reference and estimation. The left bar shows the GCI and the right one the AES estimate. The latter overpredicts the error magnitude by approximately factor 5.

Despite surface pressure distribution being the sole base for the computation of the aerodynamic coefficients, it is of interest to look at the flow field above the wing. After all, C_P is the footprint of the flow dy-

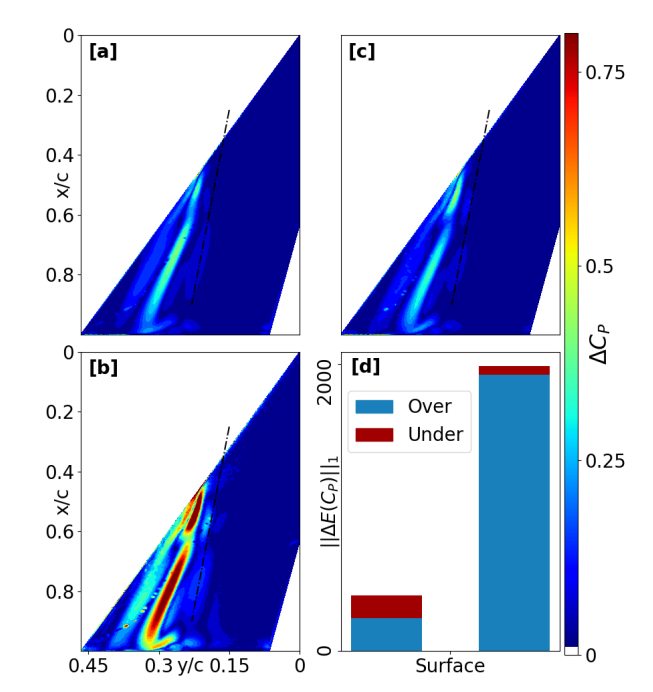


FIG 10. Contour of the surface pressure coefficient error.[a] shows the reference error, [b] the estimation using GCI and [c] the error approximated by the AES method. [d] shows the norm of difference for the two error estimations. The left bar represents the GCI and the right one the AES.

namics. Figure 11 shows a slice through the flow field x/c = 0.9 near the trailing edge. The top contour displays the vorticity magnitude obtained from the simulation on the reference mesh. One can clearly identify the strong outboard vortex and the weaker primary inboard vortex at a span-wise location y/c = -0.26. The three contours 11 [b]-[d] visualise from top to bottom the reference error, grid convergence index and approximate error scaling estimate. As previously shown for the surface pressure, both error approximations capture the error with great detail. Errors are primarily located at the leading edge where the shear layers starts to roll up and at the location of the primary cortex, since coarse grids have difficulties resolving it. Visual inspection leads to the conclusion that the GCI and AES method manage to predict the error magnitude with good accuracy.

Finally, the quantitative analysis is carried out for the flow field above the wing at different stream-wise locations. The ℓ_1 -norm for the difference between the reference and estimate error in vorticity ω is displayed in Figure 12. The left bar represents the estimate from the GCI and the right bar shows the estimate obtained from the AES. With an exception at x/c=0.7, the approximate error scaling method provides the more accurate prediction of the total error magnitude. In addition, AES has a larger portion of error that is overestimated compared to the GCI. Therefore, it can be concluded that the AES provides a more conservative estimation.

CC BY-SA 4.0

7

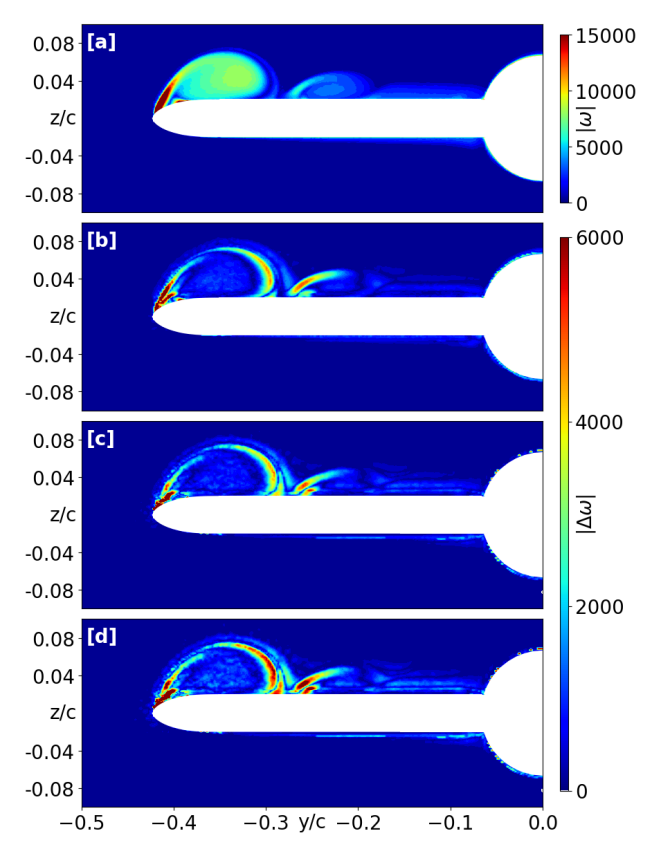


FIG 11. Vorticity contour plot at x/c=0.9 [a] and absolute vorticity error contour at x/c=0.9 for the reference error [b], GCI [c] and the AES method [d].

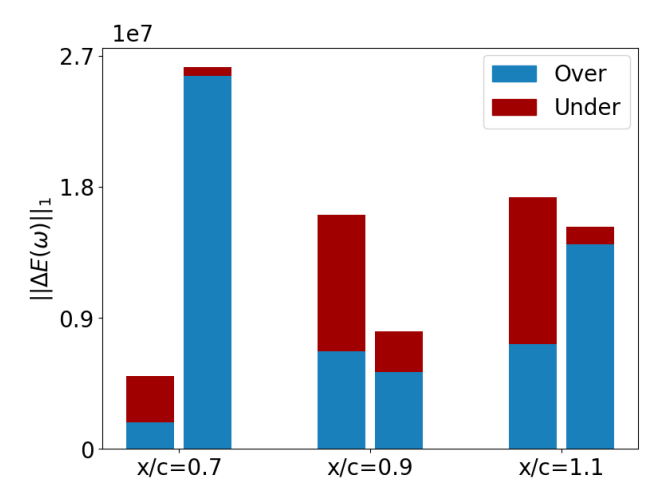


FIG 12. Summation norm of difference between reference and estimated error for three selected stream-wise locations. The left bar represents the GCI and the right bar the AES estimation.

6. SUMMARY AND CONCLUSION

The proposed estimation procedure "local GCI" fails to give a reasonable error estimate. The other two investigated methods show potential for practical implementation of error estimation into the CFD workflow. It has been shown that the algorithms can provide useful insights into discretisation errors, even if not all formal conditions for the application are met.

Areas with significant error can be identified. Even though the error magnitude can be difficult to predict correctly, it is safe to say that the procedure lays a solid ground for grid improvement. Both methods have benefits and drawbacks. While the GCI index only needs two meshes to estimate the error, it requires the determination of a typical cell size. The influence of complex geometries and local refinement through mesh size based weighting could be investigated in the future for a more accurate cell size determination. The AES method on the other hand, neglects the use of both order of convergence and cell size. Instead, it relies on solutions on three different meshes, making it computationally more expensive. Throughout the test cases, a scheme arises where the AES method overestimates the error magnitude, especially for the surface pressure distribution and Mach number error. This is backed by Figures 7, and 10. However, for error estimation, decent overprediction of the error is not necessarily a bad thing, rather it leads to a more conservative result.

Finally, it can be said that the accurate prediction of discretisation errors still remains a major challenge, even for simple turbulent flows. The methods are able to localise regions of significant discretisation error. To reach the requirements for error estimation set out by Cary et al. [3] for complex configurations, extensive effort will be required, especially to accurately predict the error magnitude.

One ongoing investigation focuses on error estimation using a single grid, but numerical schemes with varying order. This would supersede the difficult task of grid generation and simultaneously eliminate the interpolation error.

Contact address:

robin.moersch@unibw.de

References

- P. J. Roache. Verification and Validation in Computational Science and Engineering, volume 895.
 Hermosa Albuquerque, NM, 1998.
- [2] W. L. Oberkampf and Trucano T. G. Verification and validation in computational fluid dynamics. Progress in Aerospace Sciences, 38(3):209– 272, 2002.
- [3] A. W. Cary, J. Chawner, E. P. Duque, W. Gropp, W. L. Kleb, R. M. Kolonay, E. Nielsen, and B. Smith. Cfd vision 2030 road map: Progress and perspectives. In AIAA aviation 2021 forum, page 2726, 2021.
- [4] P. J. Roache. Perspective: A Method for Uniform Reporting of Grid Refinement Studies. Journal of Fluids Engineering, 116(3):405–413, 09 1994.
- [5] I. Celik, E. Karaismail, and D. Parsons. A reliable error estimation technique for cfd applica-

- tions. In AVT-147 Symposium on Computational Uncertainty in Military Vehicle Design, 2007.
- [6] F. Stern, R. V. Wilson, H. W. Coleman, and E. G. Paterson. Comprehensive Approach to Verification and Validation of CFD Simulations—Part 1: Methodology and Procedures. Journal of Fluids Engineering, 123(4):793–802, 07 2001.
- [7] L. Eça and M. Hoekstra. A procedure for the estimation of the numerical uncertainty of cfd calculations based on grid refinement studies. Journal of Computational Physics, 262:104–130, 04 2014.
- [8] L. Eça, M. Hoekstra, and P. J. Roache. Verification of calculations: An overview of the 2nd lisbon workshop. 06 2005.
- [9] L. F. Richardson and J. A. Gaunt. Viii. the deferred approach to the limit. Philosophical Transactions of the Royal Society of London. Series A, 226(636-646):299–361, 1927.
- [10] I. Celik, J. Li, G. Hu, and C. Shaffer. Limitations of Richardson Extrapolation and Some Possible Remedies. Journal of Fluids Engineering, 127(4):795–805, 04 2005.
- [11] M. D. Salas. Some observations on grid convergence. Computers & Fluids, 35(7):688–692, 2006.
- [12] D. Schwamborn, T. Gerhold, and R. Kessler. Dlrtau code an overview. In 1st ONERA/DLR Aerospace Symposium, Paris, 21.-24. Juni 1999, pages S4-2-S4-10, 1999.
- [13] P. R. Spalart and S. R. Allmaras. A one-equation turbulence model for aerodynamic flows. In 30th aerospace sciences meeting and exhibit, page 439, 1992.
- [14] S. R. Allmaras and F. T. Johnson. Modifications and clarifications for the implementation of the spalart-allmaras turbulence model. In Seventh international conference on computational fluid dynamics (ICCFD7), volume 1902, pages 1–11, 2012.
- [15] J. W. Naughton, S. Viken, and D. Greenblatt. Skin friction measurements on the nasa hump model. AIAA Journal, 44(6):1255–1265, 2006.
- [16] C. Rumsey. Turbulence modeling resource. https://turbmodels.larc.nasa.gov/. accessed on 17 September 2024.
- [17] P. Balakumar, P. S. Iyer, and M. R. Malik. Turbulence simulations of transonic flows over an naca-0012 airfoil. In AIAA SCITECH 2023 Forum, page 0254, 2023.
- [18] K. M. Luckring and D. Hummel. What was learned from the new vfe-2 experiments. Aerospace Science and Technology, 24(1):77–88, 2013.